Materials Today Energy 51 (2025) 101914

Contents lists available at ScienceDirect

Materials Today Energy

journal homepage: www.journals.elsevier.com/materials-today-energy/

Enhancing the cycling performance of sulfide-based all-solid-state lithium batteries via molecular weight-dependent fibrillation of PTFE binders

Young-Jun Lee [a,1], Se-Yeon Kim [b,1], Won-Jae Song [a], Jiho Cha [a], Dong-Won Kim [a,b,*]

[a] Department of Chemical Engineering, Hanyang University, Seoul, 04763, Republic of Korea
[b] Department of Battery Engineering, Hanyang University, Seoul, 04763, Republic of Korea

ARTICLE INFO

Keywords:
Dry-processed composite cathode
All-solid-state lithium battery
Argyrodite
Polytetrafluoroethylene binder
Molecular weight

ABSTRACT

Sulfide-based all-solid-state lithium batteries offer greater safety and higher energy density than lithium-ion batteries. An appropriate polymer binder for composite cathodes must be selected to ensure stable interfacial contact and minimize electrical resistance. Polytetrafluoroethylene (PTFE) binders, commonly used in solvent-free dry processes, undergo fibrillation under shear force to bind the cathode components. However, insufficient fibrillation and aggregation can compromise the mechanical and electrical integrity of the composite cathode, deteriorating cycling performance. In this study, we investigated the effect of PTFE molecular weight (MW) on the fibrillation behavior of the binder in composite cathodes. High-MW PTFE exhibited superior fibrillation and cohesion of the cathode components, enhanced mechanical properties, and reduced internal resistance. Consequently, the Li-In/Li_6PS_5Cl/$LiNi_{0.82}Co_{0.10}Mn_{0.08}O_2$ cell employing highly fibrillated PTFE achieved a high discharge capacity of 209.7 mAh g^{-1} (4.72 mAh cm^{-2}) at 0.05 C and good capacity retention of 97.4 % after 300 cycles at 30 °C and a rate of 0.5 C.

1. Introduction

The continuous advancement and widespread adoption of mobile electronics and electric vehicles have significantly increased the demand for lithium-ion batteries (LIBs) [1–3]. However, LIBs with flammable liquid electrolytes face challenges in increasing the energy density and pose inherent safety risks, including thermal runaway [4–6]. In this respect, all-solid-state lithium batteries (ASSLBs) have attracted significant attention because of their enhanced safety and higher energy density compared to conventional LIBs [7–10]. Among various solid electrolyte systems, sulfide electrolytes are particularly promising due to their high ambient-temperature ionic conductivities and favorable processability, enabling large-scale battery production [11–15]. However, to successfully develop ASSLBs using sulfide-based solid electrolytes, several technical challenges must be overcome [16,17]. One critical aspect is the fabrication of composite cathodes, which can be achieved using either the wet slurry or solvent-free dry process. Compared to the wet process, the dry process uses no organic solvents that cause side reactions with sulfide electrolytes. This helps maintain the high ionic conductivity of solid electrolytes within the composite cathode and also enables the fabrication of composite electrodes with high active mass loading [18–21]. Additionally, the dry process is compatible with existing roll-to-roll production techniques, making it advantageous for large-scale manufacturing [22]. In dry processes, polytetrafluoroethylene (PTFE), which undergoes fibrillation under shear stress, is commonly used to fabricate composite cathodes [19,20,23]. The strong electronegativity difference in the C–F bonds of PTFE weakens the van der Waals interactions between the polymer chains. Consequently, under an applied shear force, the polymer chains are pulled apart readily, forming PTFE fibers [24]. Networks of these fibers in the composite cathode help maintain interfacial contact between the cathode components during repeated cycling. However, insufficient fibrillation or aggregation of the polymer binder can deteriorate the mechanical and electrochemical properties of composite cathodes. Although some studies have investigated the cycling performance of PTFE-based cell in relation to physicochemical properties of PTFE, such as crystallinity and particle size [25,26], few studies have explored the effect of PTFE fibrillation on the mechanical and cycling performance of composite cathodes for ASSLBs. Lee et al. reported that $LiNi_{0.8}Mn_{0.1}Co_{0.1}O_2$ composite cathode using crystalline PTFE exhibited improved cycling and rate performance in ASSLBs, as the highly crystalline PTFE provided robust mechanical properties to the composite cathode [25]. The effect

---

* Corresponding author. Department of Chemical Engineering, Hanyang University, Seoul, 04763, Republic of Korea.
E-mail address: dongwonkim@hanyang.ac.kr (D.-W. Kim).

[1] Y.-J. Lee and S.-Y. Kim equally contributed to this work.

https://doi.org/10.1016/j.mtener.2025.101914
Received 17 March 2025; Received in revised form 30 April 2025; Accepted 10 May 2025

of PTFE particle size has also been investigated to reduce resistance and achieve a more uniform distribution. Adjusting the PTFE particle size to a few micrometers enhanced both ionic and electronic conductivities by minimizing the contribution of insulating components within the composite cathode [26].

In this study, we present a comprehensive study of dry-processed composite cathodes using PTFE for ASSLBs, with a particular focus on the degree of PTFE fibrillation. For this purpose, we fabricated composite cathodes using three types of PTFE and found that the molecular weight (MW) is a critical factor influencing fibrillation. High-MW PTFE exhibited greater fibrillation and a more uniform distribution within the composite cathode. Consequently, the composite cathodes incorporating high-MW PTFE demonstrated lower electrical resistances and superior mechanical properties than those using low-MW PTFE. The all-solid-state cell employing Li_6PS_5Cl as the solid electrolyte and $LiNi_{0.82}Co_{0.10}Mn_{0.08}O_2$ as the composite cathode with high-MW PTFE delivered a high discharge capacity of 209.7 mAh g^{-1} at 0.05 C and exhibited a good capacity retention of 97.4 % after 300 cycles at 0.5 C and 30 °C. Our study provides valuable guidance for the selection of an appropriate binder to achieve good mechanical and electrochemical properties in dry-processed composite cathodes, thereby contributing to the development of high-performance sulfide-based ASSLBs.

2. Material and methods

2.1. Materials

Two types of Li_6PS_5Cl (LPSCl, $D_{50} = 1$ and 3 μm) were purchased from POSCO JK Solid Solution Co., Ltd. The 3-μm LPSCl powder was used to make the solid electrolyte pellets, and the 1-μm LPSCl particles were employed to fabricate the composite cathodes. $LiNi_{0.82}Co_{0.10}Mn_{0.08}O_2$ (NCM, $D_{50} = 4$ μm) was kindly supplied by L&F Co., Ltd. Three types of PTFE with different MWs were purchased from Sigma Aldrich, CNP Solutions, and Solvay and denoted as PTFE(L), PTFE(M), and PTFE(H), respectively, in the order of increasing MW. Super C was supplied by Timcal Co., Ltd. Li foil (200 μm, Honjo Metal) and In foil (100 μm, Nilaco) were used as anodes.

2.2. Electrode preparation and solid-state cell assembly

The dry mixture for preparing the composite cathode was prepared by mixing NCM, LPSCl, Super C, and PTFE with a ratio of 80.0:17.5:1.5:1.0 by weight. The mixture was blended using a mortar and pestle at room temperature for 1 h. The resulting dough-like mixture was pressed using a roll-process machine (WCRP-1015HG) to induce PTFE fibrillation. The resulting freestanding composite cathode was shaped into a disc with a diameter of 13 mm. The composite cathode exhibited a specific NCM mass of 22.5 mg cm^{-2}. The all-solid-state cells were fabricated as follows: Initially, 150 mg of LPSCl powder was pelletized by cold pressing at 105 MPa in a 13 mm die made of poly (ether ether ketone). The composite cathode was then placed on an LPSCl pellet. Subsequently, they were pressed at 430 MPa. The anode was positioned on the side opposite the LPSCl pellet. Al and Ni foils were used as the current collectors for the cathode and anode, respectively. Finally, the cells were fabricated at a stack pressure of 70 MPa. Electrode fabrication and solid-state cell assembly were accomplished in an Ar atmosphere glove box (H_2O, $O_2 < 0.1$ ppm, MBRAUN).

2.3. Electrochemical measurements

The galvanostatic intermittent titration technique (GITT) was performed at a current density of 2.25 mA cm^{-2} using a WBCS 3000 (WonATech) apparatus. The cell underwent repeated discharge pulses for 60 s, followed by 60 min rest until the potential decreased to 2.4 V. The active surface area of the cathode active material could be calculated using the equation (1) [27],

$$D_{Li^+} = \frac{4}{\pi\tau}\left(\frac{m_{NCM}\,V_M}{M_{NCM}\,S}\right)^2\left(\frac{\Delta E_s}{\Delta E_t}\right)^2 \tag{1}$$

where D_{Li+} and τ indicate the diffusion coefficient of Li^+ ions and the pulse duration (60 s), respectively; m_{NCM}, V_M, and M_{NCM} represent the mass loading, molar volume, and MW of the active material, respectively; S is the active surface area of the active material; ΔE_s and ΔE_t denote the steady-state and the transient voltage changes, respectively. The direct-current internal resistance (DC-IR) was measured using the following procedure: First, the cell underwent a pre-conditioning cycle at 0.05C between 2.4 and 3.7 V. It was subsequently charged to 3.1 V and allowed to rest for 1 h. Next, charge and discharge pulses were applied at progressively increasing current rates for 10 s each, followed by a 20 min rest period. The alternating-current (AC) impedance of the stainless steel (SS)/composite cathode/SS cell was measured using an impedance analyzer over the frequency range of 10 mHz–1 MHz. The electronic and ionic conductivities of the composite cathodes were determined from the AC impedance spectra using a transmission line model [28]. For this analysis, the composite cathodes were fabricated using NCM, LPSCl, and PTFE binder, without the addition of Super C, to eliminate the influence of conductive carbon. The cycling performance of the cells was evaluated at 30 °C and 0.5 C. After subjecting the pre-conditioning cycle at 0.05 C, the cell was charged to 3.7 V at a constant current rate of 0.5 C, followed by a constant-voltage charge of 3.7 V until the current decreased to 0.25 C. The cell was then discharged to 2.4 V at 0.5 C. Rate capability was assessed by increasing the current rate from 0.1 to 2.0 C.

2.4. Characterization

The chemical structure of PTFE was investigated by Fourier-transform infrared (FTIR) spectroscopy using a Nicolet iS50 spectrometer. Differential scanning calorimetry (DSC; DSC25, TA Instruments) was performed between 0 and 370 °C at a heating and cooling rate of 5 °C min^{-1} to obtain the thermal properties of the PTFE binders. XRD patterns of PTFE were collected using a D8 ADVANCE (Bruker) diffractometer. The surface and cross-sectional structures of the PTFE membranes and composite cathodes were analyzed by field-emission scanning electron microscopy (FE-SEM; Verios G4UC). Time-of-flight secondary-ion mass spectrometry (TOF-SIMS) was performed using a TOF SIMS 5 system to analyze the distribution of PTFE fibers in the composite cathode, with an imaging area of 25 × 25 μm. The cohesive properties of the composite cathodes were examined using a surface and interfacial cutting analysis system (SAICAS, Daipla Wintes). Measurements were conducted using a diamond blade with a width of 1 mm. The horizontal and vertical forces acting on the blade were measured at a speed of 2.0 μm s^{-1}. Nanoindentation analyses of the composite cathodes were conducted using a NanoTest Vantage platform with a maximum load of 1.0 mN. X-ray photoelectron spectroscopy (XPS) measurements were performed to investigate the chemical composition of the composite cathode after 300 cycles using a K-$alpha^+$ spectrometer (Thermo Fisher Scientific). XPSPEAK41 software was used to fit all the spectra.

3. Results and discussion

The chemical structure of the PTFE used in this study was confirmed via FTIR spectroscopy. As shown in Fig. S1, all the PTFE binders exhibit dominant peaks at 1201 and 1150 cm^{-1} corresponding to the $–CF_2–$ stretching vibration and at 637 cm^{-1} related to the deformation vibration of the $–CF_2–$ segment, indicating that they have chemical structures identical to that of PTFE [29]. PTFE is insoluble in all solvents owing to its high chemical resistance derived from its extremely strong carbon–fluorine bonds. Therefore, determining the average MW of PTFE using gel permeation chromatography is difficult. Suwa et al. reported a correlation between the heat of crystallization (ΔH_c) determined by DSC and the number-average MW (M_n) [30]. They derived a useful equation for calculating the M_n of PTFE, which is applicable to the MW range of 5.2×10^5 to 4.5×10^7 g mol^{-1}. During DSC analysis, the cooling rate should be kept constant to accurately estimate the MW, as the heat of crystallization is influenced by the cooling rate. The value of M_n can be calculated using Suwa's equation, with ΔH_c expressed in units of cal g^{-1}, as follows:

$$M_n = \left(2.1 \times 10^{10}\right) \Delta H_c^{-5.16} \tag{2}$$

The thermal properties of PTFE were investigated using DSC to measure M_n using Suwa's equation. The DSC thermograms in Fig. S2 show that all the PTFE samples exhibit melting and crystallization peaks at approximately 340 °C and 310 °C, respectively. Using Suwa's equation, the M_n values of PTFE(L), PTFE(M), and PTFE(H) were determined to be 1.2×10^6, 1.8×10^6, and 3.2×10^6 g mol^{-1}, respectively. To validate these results, the XRD patterns of PTFE were obtained to compare the full width at half-maximum (FWHM) of the (100) crystalline peaks, because an increase in average MW correlates with an increase in crystallite size [31]. In other words, the FWHM of PTFE decreases with increasing its average MW. From the XRD patterns shown in Fig. S3, the FWHM values for the (100) peaks in PTFE(L), PTFE(M), and PTFE(H) are estimated to be 0.414, 0.322, and 0.211, respectively, confirming that the average MW increased in the order of PTFE(L), PTFE (M), and PTFE(H).

The effect of MW on the degree of fibrillation was investigated using SEM [32]. For this purpose, LPSCl powder and PTFE were dry-mixed using a mortar and pestle for 30 min and roll-pressed to form a solid electrolyte sheet. The LPSCl powder is then selectively removed by dissolving the sheet in water, as schematically illustrated in Fig. 1a. As shown in Fig. 1b–**1d**, the SEM images of the fibrous PTFE membranes after the removal of LPSCl reveal quite different morphologies depending on the PTFE MW. The membrane with PTFE(L) exhibited a nonuniform morphology with irregular thickness and large agglomerates. Although the PTFE(M) membrane exhibited a relatively uniform fibrous structure compared to the PTFE(L) membrane, the node-like clusters among the fibers resulted in the formation of discontinuous fibers. The membrane prepared with PTFE(H) exhibited the most uniform fibrous morphology with few agglomerates, showing a network of thread-like fibers. It has been well known that the average MW controls the chain entanglement and chain length, which directly affects how the material behaves under mechanical stress. The higher the MW, the easier it is for PTFE to fibrillate because the chains are long enough to sustain and propagate fibril formation. Based on these results, the degree of fibrillation can be correlated with the MW of PTFE; that is, the larger the MW of PTFE, the higher the fibrillation, as schematically illustrated in Fig. 1e.

To further investigate the MW-based PTFE fibrillation in composite cathodes, SEM images of the composite cathodes with different PTFE binders were analyzed. As the MW of the PTFE increased, the binder formed thinner and more uniform fibers in the composite cathode (Fig. S4). In addition, TOF-SIMS analysis was carried out to examine the distribution of the PTFE binder in the composite cathode. The NiO_2^-, Cl^-, and F^- maps in the cathodes are presented in Fig. 2. In these maps, the NiO_2^-, Cl^-, and F^- signals originate from NCM, LPSCl, and PTFE, respectively. The homogeneous distribution of NiO_2^- and Cl^- in the composite cathode demonstrated the uniform dispersion of NCM and LPSCl regardless of the MW of the PTFE binder. However, the F^- signal arising from PTFE showed different distributions depending on the MW of PTFE. PTFE with a lower MW tended to aggregate into thick fibers, whereas higher-MW PTFE was uniformly distributed within the composite cathode. These results indicate that higher-MW PTFE was fibrillated more readily and was more uniformly distributed in the composite cathode without agglomeration, which are consistent with results in

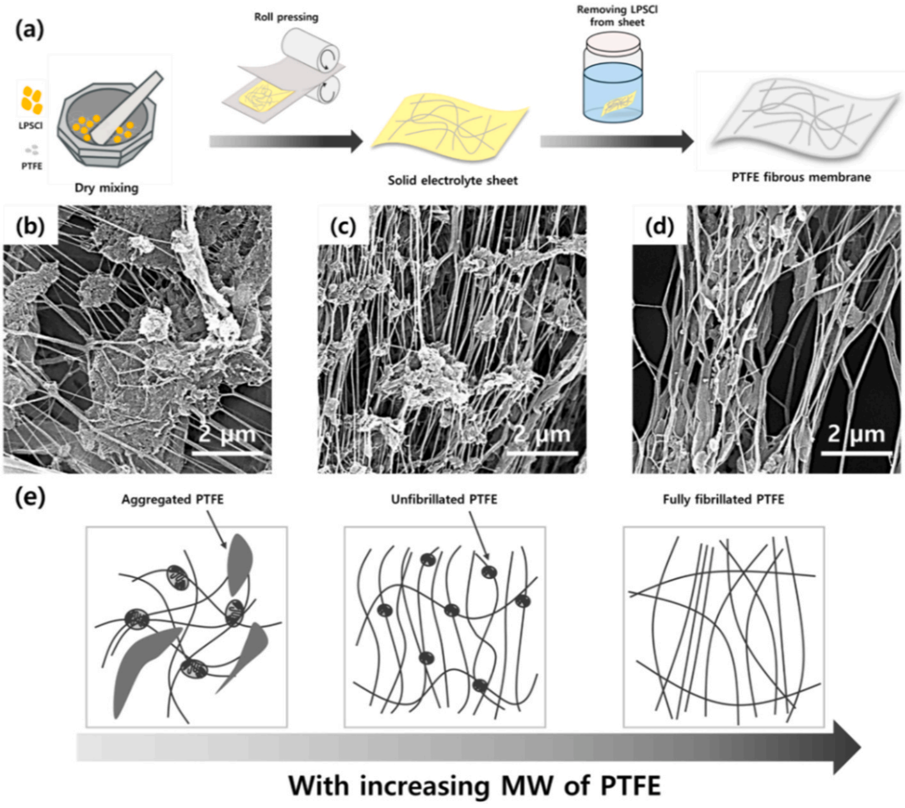

Fig. 1. (a) Preparation of solid electrolyte sheet by dry processing and removing LPSCl from the sheet to obtain the fibrous PTFE membrane. SEM images of fibrous PTFE membrane fabricated with (b) PTFE(L), (c) PTFE(M), and (d) PTFE(H). (e) Schematic illustrations comparing the degree of PTFE fibrillation according to its MW.

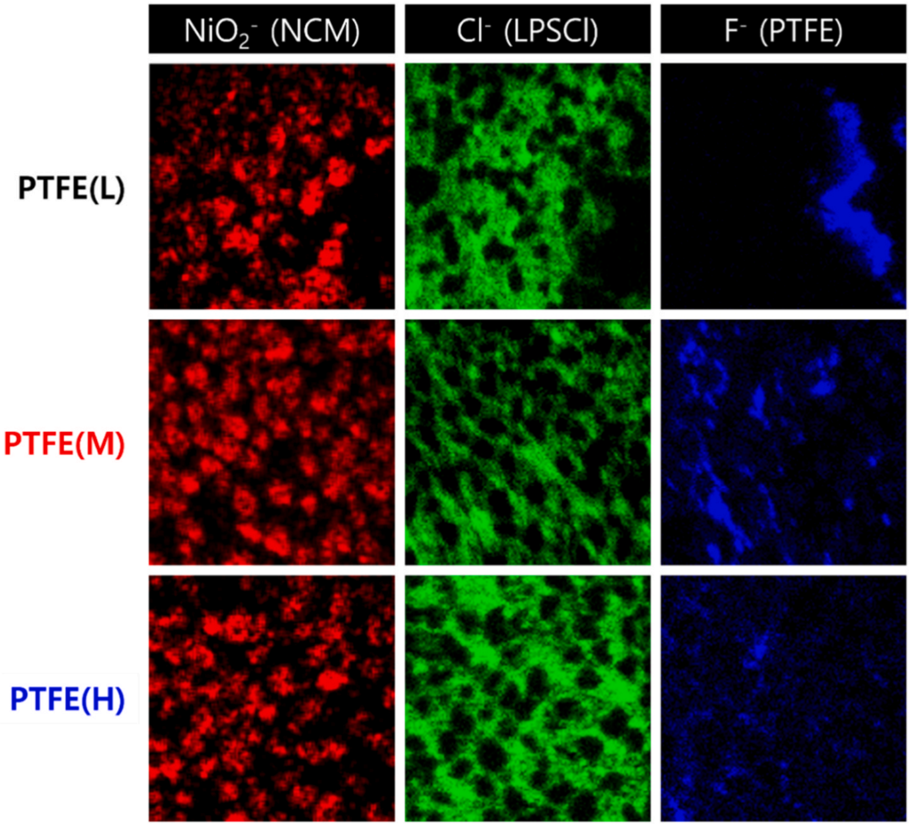

Fig. 2. TOF-SIMS mapping images of NiO$_2^-$, Cl$^-$, and F$^-$ in the composite cathodes using different PTFE binders.

Fig. 1.

SAICAS experiments were performed to compare the cohesive strengths of the composite cathodes with different PTFE binders [33,34]. As shown in Fig. 3a, the horizontal and vertical forces are measured while cutting the middle of the composite cathode using a blade moving at a constant velocity. Fig. 3b and c show that the forces required to cut the composite cathode increase with the PTFE MW owing to the increased cohesive strength among the electrode components. Nanoindentation tests were performed to evaluate the mechanical properties of the composite cathodes. As shown in Fig. S5, the composite cathode employing PTFE(H) exhibits the smallest penetration depth, indicating the best mechanical properties [35]. These results demonstrate that the composite cathode using high-MW PTFE exhibits the highest cohesive strength and best mechanical properties owing to the strong binding of the cathode components through the homogeneously spread PTFE fibers.

The electrochemical properties of the composite cathodes with different PTFE binders were characterized. The Li$^+$ diffusion within the composite cathodes was investigated using the GITT technique [36,37]. During the experiment, the cell was discharged for 60 s at a current density of 0.5 C and rested for 60 min; the resulting voltage profiles and polarization curves from the GITT experiments are depicted in Fig. 4a. The cells featuring PTFE(H) clearly exhibited lower overpotential compared to the cells with PTFE(M) and PTFE(L). The relative active surface area of active material in the cathode was determined from the GITT results shown in Fig. 4b and Fig. S6, and the corresponding values are presented in Fig. 4c. The relative active surface area could be obtained at the same state of charge to ensure a consistent Li$^+$ diffusion coefficient within the same NCM material, using equation (1). When the surface area of the active material in the PTFE(L) cathode was set to 1.0S, the corresponding values in the PTFE(M) and PTFE(H) cathodes were determined to be 1.61S and 1.83S, respectively, as shown in Table S1, indicating that the composite cathode employing PTFE(H) had the highest active surface area to facilitate the charge-transfer reaction. The electrical conductivities of the composite cathodes are determined from the electrochemical impedance spectra of the Li$^+$-ion-blocking cells, as shown in Fig. S7 [28,38]. Fig. 4d shows the ionic and electronic conductivities obtained using the transmission line model. Clearly, the cathode employing PTFE(H) exhibited the highest ionic and electronic conductivities, ascribed to the uniformly distributed PTFE offering the least hindrance to charge transport. The internal resistance of the cells prepared with different PTFE contents was calculated from DC-IR measurements [39]. As shown in Fig. 4e and Fig. S8, the cell polarization increases with increasing current density from 0.025 to 1.0 C (0.11–4.5 mA cm^{-2}). The internal resistance of the cells is estimated from the slope of the current versus voltage plot in Fig. 4f. As expected, the internal resistance decreases with increasing PTFE MW owing to the higher electronic and ionic conductivities of the composite cathode, which is consistent with the results shown in Fig. 4c and d.

The cycling performance of the Li-In/LPSCl/NCM solid-state cells assembled with composite cathodes employing different PTFE binders was evaluated, and the results are presented in Fig. 5. The cells were initially pre-cycled at 0.05 C, followed by repeated cycling at 0.5 C and 30 °C. Fig. 5a compares the charge and discharge curves of the initial pre-cycle at 0.05 C. The cell assembled with PTFE(H) achieved the highest discharge capacity of 209.7 mAh g^{-1}, corresponding to an areal capacity of 4.72 mAh cm^{-2}. The charge and discharge curves of the cells at 0.5 C are shown in Fig. 5b and Fig. S9. Among the three cells, the cell employing PTFE(L) experienced the largest increase in overpotential with cycling. These results can be attributed to poor interfacial contact owing to the weak binding property of the PTFE(L) binder and the side reactions between NCM and LPSCl caused by the poorly distributed PTFE(L) (Fig. 2) [40]. The cycling performance of the three cells is compared in Fig. 5c. The cells showed a large difference in the initial discharge capacity, which can be attributed to the previously discussed difference in the internal resistances of the composite cathodes. When

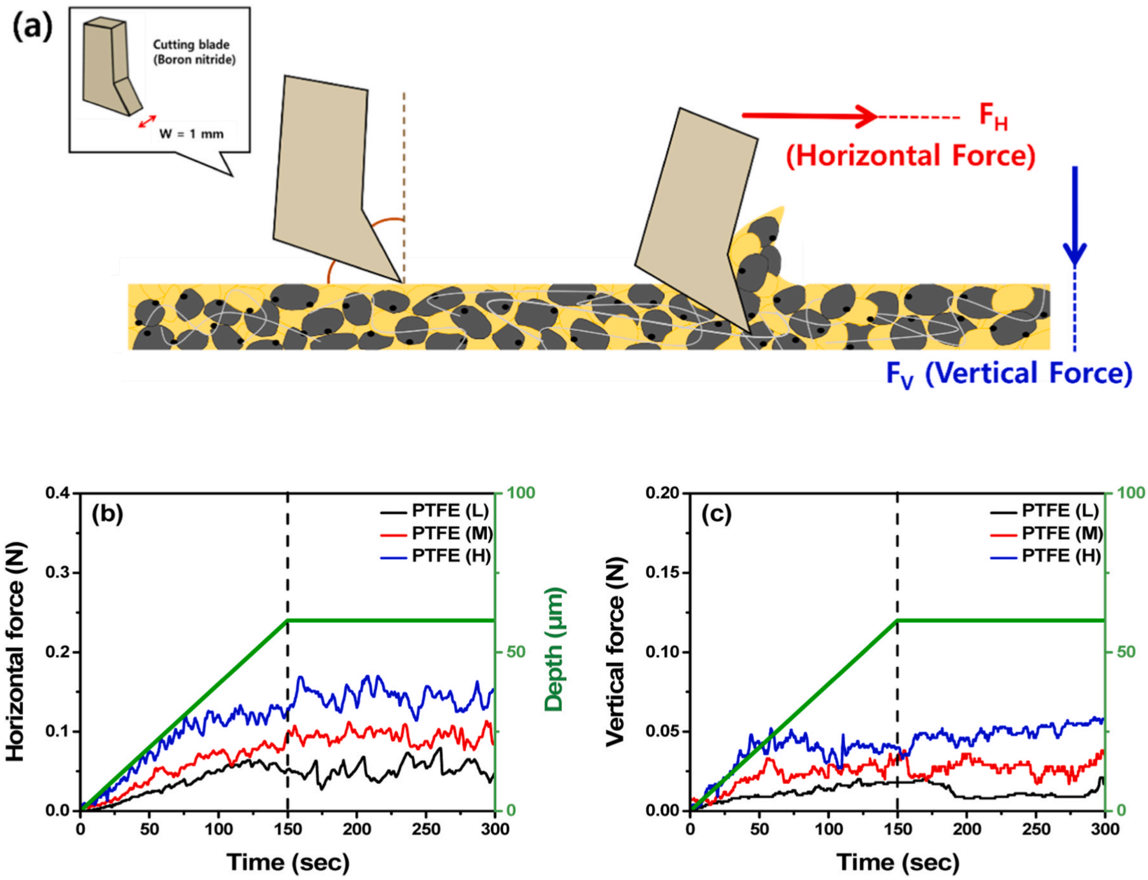

Fig. 3. (a) Schematic illustration of the SAICAS experiment. (b) Horizontal and (c) vertical cutting forces measured for composite cathodes containing PTFE(L), PTFE (M), and PTFE(H).

considering cycling stability, the degree of fibrillation according to the PTFE MW affects capacity retention. The cells with composite cathodes employing PTFE(L), PTFE(M), and PTFE(H) exhibited capacity retentions of 83.5 %, 89.3 %, and 97.4 %, respectively. Because each cell used the same solid electrolyte and anode material, the difference in capacity fading was mainly caused by the different degrees of deterioration of interfacial contact among the cathode components (NCM, LPSCl, and conductive carbon) arising from the volume changes of NCM during repeated cycling [40,41]. Accordingly, these results imply that the uniformly dispersed PTFE fibers enabled stable cycling, maintained good interfacial contact, and withstood the mechanical stress of the active materials during cycling. We fabricated a composite cathode using poly(vinylidene fluoride) (PVDF) via a dry process. As shown in Fig. S10, the cell assembled with the PVDF-based composite cathode exhibited inferior cycling stability compared to the cell with PTFE-based cathodes. In the dry process, PVDF remains as small powdery particles without fibril formation. As a result, PVDF provides much weaker cohesion, as it cannot form an interconnected network. Instead, it just sticks here and there between cathode components, not wrapping around them, leading to poor mechanical integrity and degraded electrochemical performance. The rate performance of the cells with different PTFE binders was evaluated by varying the current rates from 0.1 to 2.0 C. The discharge curves for the cells at different C rates are presented in Fig. 5d and Fig. S11, and their rate capabilities are shown in Fig. 5e. As expected from the results shown in Fig. 5c, the cell featuring PTFE(H) exhibits the best high-rate performance. Above the 2.0 C rate, it was difficult to evaluate the effect of PTFE MW on the rate performance of the cell. In our study, the solid electrolyte pellet was fabricated with a thickness of 750 μm, because the solid electrolyte was too brittle to prepare a thinner pellet. To achieve high discharge capacities at higher current rates, it is essential to reduce the thickness of the solid electrolyte pellet, as it directly impacts the internal resistance of the cell. Based on these results, the composite cathode with PTFE(H) demonstrated the best mechanical and electrochemical properties compared to those with PTFE(L) and PTFE(M) because of the high fibrillation of the binder, which resulted in superior cycling performance considering cycling stability and rate performance.

To explore the effect of the PTFE MW on the interfacial contact within the composite cathodes, cross-sectional SEM images of the cathodes were obtained before and after 300 cycles (Fig. S12 and Fig. 6). As shown in Fig. S12, all the composite cathodes showed good interfacial contact between NCM and LPSCl, with no noticeable porosity or interfacial voids. However, after cycling, a noticeable difference in the interfacial contact between NCM and LPSCl was observed to depend on the MW of the PTFE used in the composite cathode. The cathode using PTFE(L) revealed numerous large voids induced by the volume change of NCM, whereas the cathode employing PTFE(H) maintained good interfacial contact after cycling because of its strong binding and cohesive properties. These results suggest that void formation after cycling is closely related to the mechanical properties of the composite cathode, particularly its resistance to the volume changes of NCM, as confirmed from the SAICAS and nanoindentation results. These findings demonstrate that the PTFE(H)-based composite cathode possesses superior cohesive strength and mechanical robustness against external forces, leading to improved interfacial stability. The voids between NCM and LPSCl disconnected the pathways for Li^+ ion transport, leading to an increase of internal resistance and gradual capacity loss of the cell.

The chemical decomposition of LPSCl in the composite cathodes was analyzed by XPS. Fig. 7 shows the XPS spectra of the cathodes with different PTFE after 300 cycles. In the XPS spectra shown in Fig. 7a and

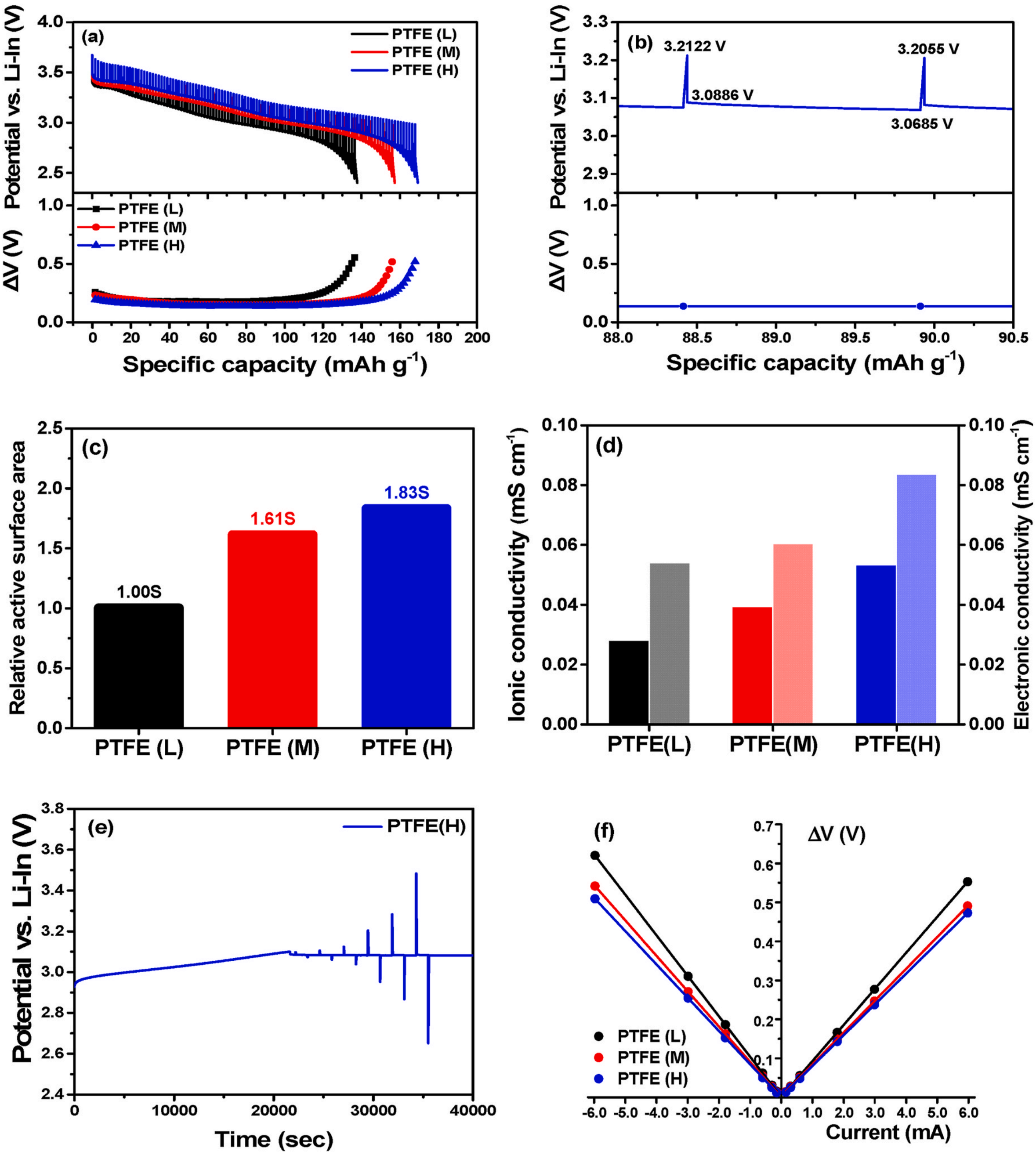

Fig. 4. (a) Voltage profiles and polarization plots of the ASSLBs with PTFE with different MWs. (b) Potential response of the cell with the cathode using PTFE(H) and (c) relative active surface area of the NMC in the composite cathodes. (d) Electrical conductivities of the composite cathodes. (e) Voltage response of the cell with PTFE(H) during the DC-IR experiment. (f) Current vs. voltage of the cells assembled using PTFE with different MWs.

b, peaks for P–S$_n$–P, SO_3^{2-}, and PO_3^{2-} can be observed, which arise from the oxidative decomposition of LPSCl [42,43]. The peak corresponding to P–S$_n$–P appeared at 163.5 and 132.9 eV in the S 2*p* and P 2*p* spectra, respectively. The SO_3^{2-} peak was observed at 167.1 eV in the S 2*p* spectrum, and the PO_3^{2-} peak was found at 134.0 eV in the P 2*p* spectrum [44–46]. The intensity ratio of each component is plotted in Fig. 7c to compare the degree of the anodic decomposition of LPSCl. The relative amounts of oxidation products such as P–S$_n$–P, SO_3^{2-}, and PO_3^{2-} increased as the PTFE MW decreased. As mentioned previously, PTFE with higher MW tended to form uniform and thin fibers within the composite cathode. Accordingly, the cell utilizing the composite cathode with high-MW PTFE exhibited low internal resistance and polarization. Such low polarization of the cell mitigated the oxidative decomposition of LPSCl at high voltages [47], which can be attributed to the superior cycling performance of the cell featuring high-MW PTFE. Our results demonstrate that the use of high-MW PTFE with high fibrillation in the composite cathode significantly enhances the cycling performance of sulfide-based ASSLBs. Based on the above results, the fibrillation of high-MW PTFE during large-scale dry mixing and roll-to-roll processing is essential for forming the mechanical network that binds the electrode, preventing fractures during bending or compression. In these processes, controlled fibrillation is necessary to achieve uniform mechanical properties within the composite electrode, stable adhesion to current collectors, and good flexibility and durability during winding or stacking. Therefore, a high degree of fibrillation is critical to ensure the scalability and reproducibility of electrode production.

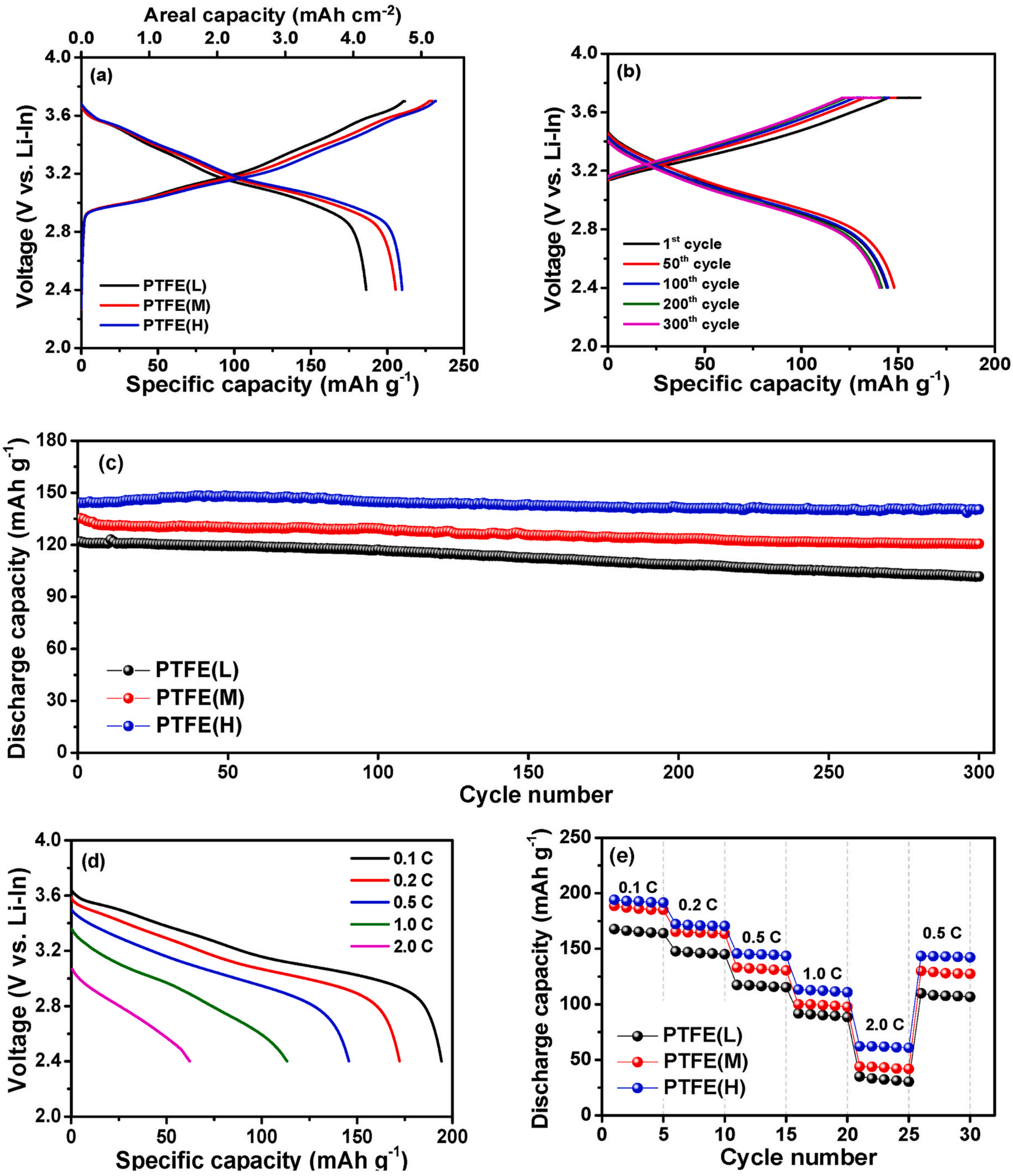

Fig. 5. (a) Cycling curves of cells with different composite cathodes during pre-cycling at 0.05 C. (b) Cycling curves of the cell with composite cathode using PTFE(H) at 0.5 C. (c) Cycling performance of the cells with different PTFE binders at 0.5 C. (d) First discharge curves of the cell with PTFE(H) at various current rates. (e) Rate capability of the cells. All tests are conducted at 30 °C.

4. Conclusions

In this study, we prepared composite cathodes for ASSLBs using PTFE binders with different MWs. As the MW of the PTFE binder increased, the binder in the composite cathode formed thinner and more uniform fibers with more effective binding of the cathode components. Consequently, the composite cathode with the high-MW PTFE exhibited superior mechanical properties and low internal resistance. The all-solid-state Li-In/LPSCl/NCM cell with high-MW PTFE delivered a high discharge capacity of 209.7 mAh g^{-1} at 0.05 C and NCM mass loading of 22.5 mg cm^{-2} (areal capacity: 4.72 mAh cm^{-2}) and revealed high cycling stability with a capacity retention of 97.4 % after 300 cycles at 0.5 C and 30 °C. Our results demonstrate that the use of high-MW PTFE in composite cathodes is beneficial for achieving good cycling performance in sulfide-based ASSLBs.

CRediT authorship contribution statement

Young-Jun Lee: Writing – original draft, Formal analysis, Data curation, Conceptualization. **Se-Yeon Kim:** Writing – original draft, Investigation, Data curation, Conceptualization. **Won-Jae Song:** Methodology, Investigation. **Jiho Cha:** Validation, Formal analysis. **Dong-Won Kim:** Writing – review & editing, Supervision, Project administration, Funding acquisition, Conceptualization.

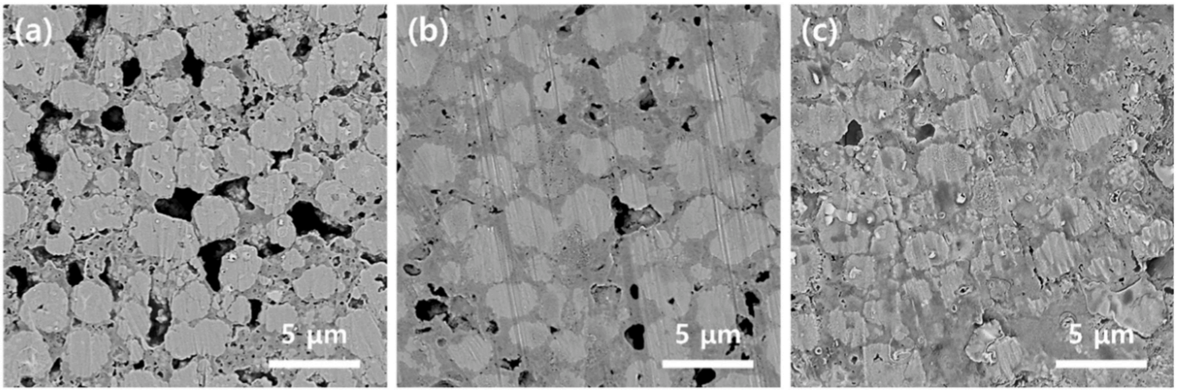

Fig. 6. Cross-sectional SEM images of the composite cathodes prepared with (a) PTFE(L), (b) PTFE(M), and (c) PTFE(H) after 300 cycles at 0.5 C and 30 °C.

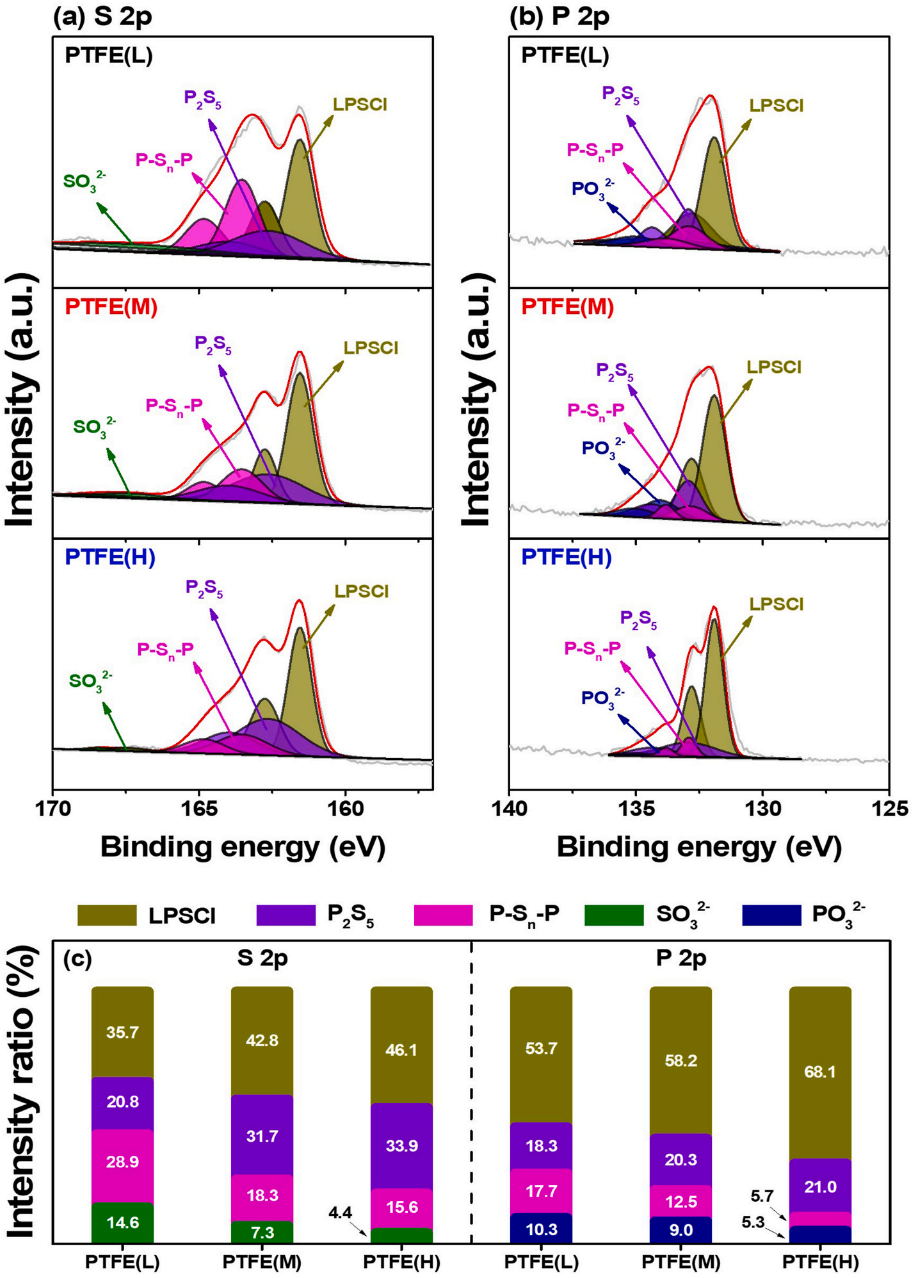

Fig. 7. XPS (a) S 2*p* and (b) P 2*p* spectra of the composite cathode using different PTFE after 300 cycles. (c) Intensity ratio of each component in the S 2*p* and P 2*p* spectra.

Declaration of competing interest

The authors declare that they have no known competing financial interests or personal relationships that could have appeared to influence the work reported in this paper.

Acknowledgments

This work was supported by the National Research Foundation of Korea (RS-2024-00454354) and Technology Innovation Program (20024827) funded by the Ministry of Trade, Industry, and Energy (MOTIE, Korea).

Appendix A. Supplementary data

Supplementary data to this article can be found online at https://doi.org/10.1016/j.mtener.2025.101914.

Data availability

Data will be made available on request.

References

[1] Z. Yang, H. Huang, F. Lin, Sustainable electric vehicle batteries for a sustainable world: perspectives on battery cathodes, environment, supply chain, manufacturing, life cycle, and policy, Adv. Energy Mater. 12 (2022) 2200383, https://doi.org/10.1002/aenm.202200383.

[2] N. Kittner, F. Lill, D.M. Kammen, Energy storage deployment and innovation for the clean energy transition, Nat. Energy 2 (2017) 17125, https://doi.org/10.1038/nenergy.2017.125.

[3] S. Chen, F. Dai, M. Cai, Opportunities and challenges of high-energy lithium metal batteries for electric vehicle applications, ACS Energy Lett. 5 (2020) 3140–3151, https://doi.org/10.1021/acsenergylett.0c01545.

[4] Y. Chen, Y. Kang, Y. Zhao, L. Wang, J. Liu, Y. Li, Z. Liang, X. He, X. Li, N. Tavajohi, B. Li, A review of lithium-ion battery safety concerns: the issues, strategies, and testing standards, J. Energy Chem. 59 (2021) 83–99, https://doi.org/10.1016/j.jechem.2020.10.017.

[5] J. Wang, Y. Yamada, K. Sodeyama, E. Watanabe, K. Takada, Y. Tateyama, A. Yamada, Fire-extinguishing organic electrolytes for safe batteries, Nat. Energy 3 (2018) 22–29, https://doi.org/10.1038/s41560-017-0033-8.

[6] H. Li, H. Wang, Z. Xu, K. Wang, M. Ge, L. Gan, Y. Zhang, Y. Tang, S. Chen, Thermal-responsive and fire-resistant materials for high-safety lithium-ion batteries, Small 17 (2021) 2103679, https://doi.org/10.1002/smll.202103679.

[7] Y. Tian, G. Zeng, A. Rutt, T. Shi, H. Kim, J. Wang, J. Koettgen, Y. Sun, B. Ouyang, T. Chen, Z. Lun, Z. Rong, K. Persson, G. Ceder, Promises and challenges of next-generation "beyond Li-ion" batteries for electric vehicles and grid decarbonization, Chem. Rev. 121 (2021) 1623–1669, https://doi.org/10.1021/acs.chemrev.0c00767.

[8] T. Famprikis, P. Canepa, J.A. Dawson, M.S. Islam, C. Masquelier, Fundamentals of inorganic solid-state electrolytes for batteries, Nat. Mater. 18 (2019) 1278–1291, https://doi.org/10.1038/s41563-019-0431-3.

[9] Y.-K. Sun, Promising all-solid-state batteries for future electric vehicles, ACS Energy Lett. 5 (2020) 3221–3223, https://doi.org/10.1021/acsenergylett.0c01977.

[10] Z. Guo, H. Zhao, Y. Xiao, S. Liang, X. Zhang, N. Wang, J. Yang, X. Huang, Recent progress of thin solid-state electrolytes and applications for solid-state lithium pouch cells, Mater, Today Energy 48 (2025) 101801, https://doi.org/10.1016/j.mtener.2025.101801.

[11] A. Manthiram, X. Yu, S. Wang, Lithium battery chemistries enabled by solid-state electrolytes, Nat. Rev. Mater. 2 (2017) 16103, https://doi.org/10.1038/natrevmats.2016.103.

[12] S. Chen, D. Xie, G. Liu, J.P. Mwizerwa, Q. Zhang, Y. Zhao, X. Xu, X. Yao, Sulfide solid electrolytes for all-solid-state lithium batteries: structure, conductivity, stability and application, Energy Storage Mater. 14 (2018) 58–74, https://doi.org/10.1016/j.ensm.2018.02.020.

[13] S.H. Kang, J.Y. Kim, D.O. Shin, M.J. Lee, Y.-G. Lee, 2D argyrodite LPSCl solid electrolyte for all-solid-state Li-ion battery using reduced graphene oxide template, Mater. Today Energy 23 (2022) 100913, https://doi.org/10.1016/j.mtener.2021.100913.

[14] Z. Moradi, A. Lanjan, R. Tyagi, S. Srinivasan, Review on current state, challenges, and potential Solutions in solid-state batteries Research, J. Energy Storage 73 (2023) 109048, https://doi.org/10.1016/j.est.2023.109048.

[15] A. Das, S. Sahu, M. Mohapatra, S. Verma, A.J. Bhattacharyya, S. Basu, Lithium-ion conductive glass-ceramic electrolytes enable safe and practical Li batteries, Mater. Today Energy 29 (2022) 101118, https://doi.org/10.1016/j.mtener.2022.101118.

[16] Y.B. Song, K.H. Baeck, H. Kwak, H. Lim, Y.S. Jung, Dimensional strategies for bridging the Research gap between lab-scale and potentially practical all-solid-state batteries: the role of sulfide solid electrolyte films, Adv. Energy Mater. 13 (2023) 2301142, https://doi.org/10.1002/aenm.202301142.

[17] Y.J. Nam, D.Y. Oh, S.H. Jung, Y.S. Jung, Toward practical all-solid-state lithium-ion batteries with high energy density and safety: comparative study for electrodes fabricated by dry- and slurry-mixing processes, J. Power Sources 375 (2018) 93–101, https://doi.org/10.1016/j.jpowsour.2017.11.031.

[18] Y. Lu, C.-Z. Zhao, H. Yuan, J.-K. Hu, J.-Q. Huang, Q. Zhang, Dry electrode Technology, the rising star in solid-state battery industrialization, Matter 5 (2022) 876–898, https://doi.org/10.1016/j.matt.2022.01.011.

[19] Y. Li, Y. Wu, Z. Wang, J. Xu, T. Ma, L. Chen, H. Li, F. Wu, Progress in solvent-free dry-film Technology for batteries and supercapacitors, Mater. Today 55 (2022) 92–109, https://doi.org/10.1016/j.mattod.2022.04.008.

[20] Y.-G. Lee, S. Fujiki, C. Jung, N. Suzuki, N. Yashiro, R. Omoda, D.-S. Ko, T. Shiratsuchi, T. Sugimoto, S. Ryu, J.H. Ku, T. Watanabe, Y. Park, Y. Aihara, D. Im, I.T. Han, High-energy long-cycling all-solid-state lithium metal batteries enabled by silver–carbon composite anodes, Nat. Energy 5 (2020) 299–308, https://doi.org/10.1038/s41560-020-0575-z.

[21] D. Lee, Y. Shim, Y. Kim, G. Kwon, S.H. Choi, K. Kim, D.-J. Yoo, Shear force effect of the dry process on cathode contact coverage in all-solid-state batteries, Nat. Commun. 15 (2024) 4763, https://doi.org/10.1038/s41467-024-49183-3.

[22] W. Jin, G. Song, J.-K. Yoo, S.-K. Jung, T.-H. Kim, J. Kim, Advancements in dry electrode technologies: towards sustainable and efficient battery manufacturing, Chemelectrochem 11 (2024) e202400288, https://doi.org/10.1002/celc.202400288.

[23] F. Hippauf, B. Schumm, S. Doerfler, H. Althues, S. Fujiki, T. Shiratsuchi, T. Tsujimura, Y. Aihara, S. Kaskel, Overcoming binder limitations of sheet-type solid-state cathodes using a solvent-free dry-film approach, Energy Storage Mater. 21 (2019) 390–398, https://doi.org/10.1016/j.ensm.2019.05.033.

[24] K. Sato, Y. Tominaga, Y. Imai, T. Yoshiyama, Y. Aburatani, Deformation capability of poly(tetrafluoroethylene) materials: estimation with X-ray diffraction measurements, Polym. Test. 113 (2022) 107690, https://doi.org/10.1016/j.polymertesting.2022.107690.

[25] D. Lee, A. Manthiram, Stable cycling with intimate contacts enabled by crystallinity-controlled PTFE-based solvent-free cathodes in all-solid-state batteries, Small Methods 7 (2023) 2201680, https://doi.org/10.1002/smtd.202201680.

[26] K. Lee, Y. Jo, J.S. Nam, H. Yu, Y.-J. Kim, Dry-film Technology employing cryo-pulverized polytetrafluoroethylene binder for all-solid-state batteries, Chem. Eng. J. 487 (2024) 150221, https://doi.org/10.1016/j.cej.2024.150221.

[27] S.-B. Hong, Y.-J. Lee, U.-H. Kim, C. Bak, Y.M. Lee, W. Cho, H.J. Hah, Y.-K. Sun, D.-W. Kim, All-solid-state lithium batteries: Li^+-Conducting ionomer binder for dry-processed composite cathodes, ACS Energy Lett. 7 (2022) 1092–1100, https://doi.org/10.1021/acsenergylett.1c02756.

[28] J.S. Nam, W.T.A. Ran, S.H. Lee, T.H.L. Vuong, H. Jo, J.-H. Lee, S.M. Hwang, Y.-J. Kim, Densification and charge transport characterization of composite cathodes with single-crystalline $LiNi_{0.8}Co_{0.15}Al_{0.05}O_2$ for solid-state batteries, Energy Storage Mater. 46 (2022) 155–164, https://doi.org/10.1016/j.ensm.2022.01.015.

[29] N. Wang, H. Wang, J. Ren, G. Gao, S. Chen, G. Zhao, Y. Yang, J. Wang, Novel additive of PTFE@SiO_2 core-shell nanoparticles with superior water lubricating properties, Mater. Des. 195 (2020) 109069, https://doi.org/10.1016/j.matdes.2020.109069.

[30] T. Suwa, M. Takehisa, S. Machi, Melting and crystallization behavior of poly (tetrafluoroethylene). New method for molecular weight measurement of poly (tetrafluoroethylene) using a differential scanning calorimeter, J. Appl. Polym. Sci. 17 (1973) 3253–3257, https://doi.org/10.1002/app.1973.070171102.

[31] J.D. Moskowitz, J.S. Wiggins, Thermo-oxidative stabilization of polyacrylonitrile and its copolymers: effect of molecular weight, dispersity, and polymerization pathway, Polym. Degrad. Stabil. 125 (2016) 76–86, https://doi.org/10.1016/j.polymdegradstab.2015.12.025.

[32] D.J. Lee, J. Jang, J.-P. Lee, J. Wu, Y.-T. Chen, J. Holoubek, K. Yu, S.-Y. Ham, Y. Jeon, T.-H. Kim, J.B. Lee, M.-S. Song, Y.S. Meng, Z. Chen, Physio-electrochemically durable dry-processed solid-state electrolyte films for all-solid-state batteries, Adv. Funct. Mater. 33 (2023) 2301341, https://doi.org/10.1002/adfm.202301341.

[33] S. Byun, J.-H. Yu, J. Choi, S. Yun, Y. Roh, C.B. Dzakpasu, S.H. Park, J.-G. Oh, B. K. Hong, Y.M. Lee, Unraveling the cohesive and interfacial adhesive strengths of electrodes for automotive fuel cells, J. Power Sources 455 (2020) 227928, https://doi.org/10.1016/j.jpowsour.2020.227928.

[34] S.-B. Hong, Y.-R. Jang, H. Kim, Y.-C. Jung, G. Shin, H.J. Hah, W. Cho, Y.-K. Sun, D.-W. Kim, Wet-processable binder in composite cathode for high energy density all-solid-state lithium batteries, Adv. Energy Mater. 14 (2024) 2400802, https://doi.org/10.1002/aenm.202400802.

[35] Y.-J. Lee, S.-B. Hong, H.-J. Lee, H.-T. Sim, Y. Kim, S. Kim, D.-W. Kim, Flexible and thin sulfide-based solid electrolyte sheet with Li+-Ion conductive polymer network for all-solid-state lithium-ion batteries, Chem. Eng. J. 477 (2023) 146983, https://doi.org/10.1016/j.cej.2023.146983.

[36] K.H. Park, D.Y. Oh, Y.E. Choi, Y.J. Nam, L. Han, J.-Y. Kim, H. Xin, F. Lin, S.M. Oh, Y.S. Jung, Solution-processable glass LiI-Li_4SnS_4 superionic conductors for all-solid-state Li-ion batteries, Adv. Mater. 28 (2016) 1874–1883, https://doi.org/10.1002/adma.201505008.

[37] D.Y. Oh, Y.J. Nam, K.H. Park, S.H. Jung, K.T. Kim, A.R. Ha, Y.S. Jung, Slurry-fabricable Li^+-Conductive polymeric binders for practical all-solid-state lithium-ion batteries enabled by solvate ionic liquids, Adv. Energy Mater. 9 (2019) 1802927, https://doi.org/10.1002/aenm.201802927.

[38] J. Cha, S. Kim, U.T. Nakate, D.-W. Kim, Highly conductive composite cathode prepared by dry process using nafion-Li ionomer for sulfide-based all-solid-state

lithium batteries, J. Power Sources 613 (2024) 234914, https://doi.org/10.1016/j.jpowsour.2024.234914.

[39] K. Lee, J. Lee, S. Choi, K. Char, J.W. Choi, Thiol–ene click reaction for fine polarity tuning of polymeric binders in solution-processed all-solid-state batteries, ACS Energy Lett. 4 (2019) 94–101, https://doi.org/10.1021/acsenergylett.8b01726.

[40] J. Kim, W. Lee, J. Seok, E. Lee, W. Choi, H. Park, S. Yun, M. Kim, J. Lim, W.-S. Yoon, Inhomogeneous lithium-storage reaction triggering the inefficiency of all-solid-state batteries, J. Energy Chem. 66 (2022) 226–236, https://doi.org/10.1016/j.jechem.2021.08.017.

[41] R. Koerver, W. Zhang, L. de Biasi, S. Schweidler, A.O. Kondrakov, S. Kolling, T. Brezesinski, P. Hartmann, W.G. Zeier, J. Janek, Chemo-mechanical expansion of lithium electrode materials – on the route to mechanically optimized all-solid-state batteries, Energy Environ. Sci. 11 (2018) 2142–2158, https://doi.org/10.1039/C8EE00907D.

[42] Y. Han, S.H. Jung, H. Kwak, S. Jun, H.H. Kwak, J.-H. Lee, S.-T. Hong, Y.S. Jung, Single- or poly-crystalline Ni-rich layered cathode, sulfide or halide solid electrolyte: which will be the winners for all-solid-state batteries? Adv. Energy Mater. 11 (2021) 2100126 https://doi.org/10.1002/aenm.202100126.

[43] S.H. Jung, U.-H. Kim, J.-H. Kim, S. Jun, C.S. Yoon, Y.S. Jung, Y.-K. Sun, Ni-rich layered cathode materials with electrochemo-mechanically compliant microstructures for all-solid-state Li batteries, Adv. Energy Mater. 10 (2020) 1903360, https://doi.org/10.1002/aenm.201903360.

[44] K.H. Park, Q. Bai, D.H. Kim, D.Y. Oh, Y. Zhu, Y. Mo, Y.S. Jung, Design strategies, practical considerations, and new solution processes of sulfide solid electrolytes for all-solid-state batteries, Adv. Energy Mater. 8 (2018) 1800035, https://doi.org/10.1002/aenm.201800035.

[45] J. Auvergniot, A. Cassel, D. Foix, V. Viallet, V. Seznce, R. Dedryvere, Redox activity of argyrodite Li_6PS_5Cl electrolyte in all-solid-state Li-ion battery: an XPS study, Solid State Ionics 300 (2017) 78–85, https://doi.org/10.1016/j.ssi.2016.11.029.

[46] J. Auvergniot, A. Cassel, J.-B. Ledeuil, V. Viallet, V. Seznec, R. Dedryvere, Interface stability of argyrodite Li_6PS_5Cl toward $LiCoO_2$, $LiNi_{1/3}Co_{1/3}Mn_{1/3}O_2$, and $LiMn_2O_4$ in bulk all-solid-state batteries, Chem. Mater. 29 (2017) 3883–3890, https://doi.org/10.1021/acs.chemmater.6b04990.

[47] H.-J. Shin, J.T. Kim, A.-Y. Kim, N. Noh, J. Park, C.R. Park, S. Yu, H. Kim, K. Y. Chung, J.M. Yuk, S.-T. Myung, H.-G. Jung, New consideration of degradation accelerating of all-solid-state batteries under a low-pressure condition, Adv. Energy Mater. 13 (2023) 2301220, https://doi.org/10.1002/aenm.202301220.